Numerical Analysis of Multirotor Aerodynamic Interactions in One-After-Another Configuration

Kangni Combey[1,2], Khaoula Qaissi[1], Mustapha Faqir[1]and Omer A. Elsayed[1]

[1]School of Aerospace and Automotive Engineering, College of Engineering and Architecture, LERMA Lab, International University of Rabat, Morocco
[2]*kangni.combey@uir.ac.ma*

Abstract

Electric vertical take-off and landing (eVTOL) aircraft powered by distributed electric propulsion (DEP) systems are emerging as a promising solution for urban air mobility (UAM). However, the intricate aerodynamic interactions between multirotor in close proximity pose significant design challenges that must be addressed during the conceptual design phase. This study employs a combination of unsteady Reynolds-Averaged Navier-Stokes (URANS) and Large Eddy Simulation (LES) to comprehensively evaluate propeller– propeller aerodynamic interactions in One-After-Another (OAA) configuration. The simulation starts with the URANS couple with SST $k-\omega$ turbulence model as a solution starter, and after a sufficient level of convergence is reached, it is superimposed by the LES turbulence model. This approach allows us to capture the complicated flow physics associated with multirotor interactions. The study began by measuring the performance of an isolated propeller to provide a reference point for the effect of these interactions on the overall performance. The computational model was validated against experimental data, showing good agreement and demonstrating the accuracy of the model. The investigation reveals that the aft propeller in the OAA configuration experiences a thrust reduction of up to 12% when partially overlapped and at zero propeller angle, with a lateral spacing of 1.4 times the propeller radius $(1.4R_p)$ and a longitudinal spacing of 2.66 times the propeller radius $(2.66R_p)$. This reduction is attributed to the non-uniform incoming flow resulting from the interaction with the wake region of the front propeller. Furthermore, this research focuses on the evolution of propeller slipstreams and their intricate interactions, thus offering an understanding of the aerodynamic complexities of multirotor systems. Overall, this research contributes to ongoing efforts to fully characterize the aerodynamic interactions of multirotor systems to enable practical eVTOL transportation.

Keywords : eVTOL Aircraft, Aerodynamics Interactions, Multirotor, One-After-Another Configuration, Urban Air Mobility

1 Introduction

Scientific and technological evolution has led to a surge in energy requirements, urbanisation and a growing number of vehicles on roads. Among the issues stemming from high numbers of vehicles on the roads is traffic congestion, causing longer and delays travel times and higher carbon emissions and exacerbating climate problems. To tackle both energy scarcity and mitigate climate change impacts, it is feasible to envision a future of transportation that embraces green technologies, specifically electric alternative to fossil fuels. Public transportation systems like buses and high-speed trains can help alleviate these issues by adopting enhanced electrical technology and with appropriate transit infrastructure. However, in densely populated cities with limited space for new infrastructure development, relying solely on green terrestrial public transport may not offer a comprehensive solution. Consequently, the concept of Urban Air Mobility (UAM) has emerged, wherein intercity and intracity transportation will be facilitated by Electric Vertical Take-Off and Landing (eVTOL) aircraft [1, 2]. eVTOL has emerged as potential solution to address the increasing demand for UAM. These innovative aircraft are being designed to operate a large range of missions, including upon request taxi services [3], air ambulances, emergency supply delivery, organ transport [4], and scheduled airline excursions. The eVTOLs aircraft employ Distributive Electric Propulsion (DEP) system [5, 6], incorporating multirotor and with small diameter propellers to reduce noise, local emissions

and cost of the aircraft [7]. Furthermore, these air vehicles only require start and end points infrastructures, called vertiports, reducing therefore the cost of infrastructure. The concept of air vehicles is a game changer and a potential alternative for transportation in mega-cities and metropolitan area as they offer more flexible trajectories than cars and trains [7]. For instance, according to Uber technical report, one-way trip from San Francisco to San Jose with eVTOL would take as little as 15 minutes, compared to 1 hour 40 min by car [3]. The DEP system employed by the eVTOL, incorporates multirotor and propellers to reduce noise while maintaining the power output compared to larger single propellers. Propeller system are used because these vehicles operate at low altitudes. At lower altitudes, the propeller engine has been found to be more effective than other propulsive systems such as turbofans and turbojets [8]. The rotating blades produce lift, which is required to propel the aircraft into the air [9]. Whereas there were only a few dozen eVTOL aircraft concepts in 2016, there are now approximately 1000 registered eVTOLs aircraft concepts according to World eVTOL Aircraft Directory [10]. All known electric and hybrid-electric vertical takeoff and landing concepts are classified into five groups based on how their thrusters work : Vectored Thrust, Lift + Cruise, Wingless (Multicopter), Electric Rotorcraft (eHelos) and Hoverbikes [11].

In light of the promising advantages presented by eVTOL aircraft, it is imperative to address the intricate aerodynamics and aeroacoustics interactions that arise from the use of multirotor configurations [12]. These interactions, including rotor-rotor, rotor-body, and rotor-lifting surface interactions, demand careful consideration throughout the aircraft design phase.

For many years, there has been a growing interest in integrating propellers onto wings. William Hayes' pioneering study showed the potential for enhanced thrust created by the rear propeller when it overlaps with the front propeller [13]. However, Usai Daniele's [14] and Stokkermans [15] experiments indicated that when fully overlapped, a propeller operating in a non-uniform inflow and ingesting the wake of another propeller could face a significant thrust loss of up to 80%. Experimental investigation conducted by Abraham Atte et al. [16] further demonstrates that a tandem configuration's aft rotor experiences a significant 24% decrease in thrust coefficient when compared to a single rotor operating at the same rotational speed and airspeed with a hub spacing of 2.1 times the propeller radius ($2.1R_p$). In a numerical study, R. Piccinini et al. [17] revealed that side-by-side (SBS) configurations exhibited a slight performance decrease, while tandem configurations experienced a more substantial reduction. Full overlap of propeller disks resulted in a notable 30% thrust loss and a 20% reduction in propulsive efficiency. Stokkermans [18] found that in SBS configuration, interaction effects become particularly severe as the propeller angle of attack increases, leading to a significant reduction in rear propeller thrust, up to 30%, at a constant advance ratio (J). Moreover, an extensive investigation carried out by A. Zarri et al. [19], highlighted the phenomenon of tip-on-tip interaction. Therefore, an accurate assessment of these interactions during the conceptual design phase is crucial for precise performance predictions.

One promising approach to mitigate these challenges is the implementation of advanced flow control methods. Flow control have shown considerable promise in enhancing the aerodynamics of propulsion systems. These devices, both active and passive, can effectively prevent or delay flow separation and suppress turbulence, reduce the wake intensity or redirect the wake away in the downwind. The utilization of such flow control strategies has been demonstrated in several studies. [20, 21, 22, 23, 24, 25].

Although substantial research has delved into propeller interactions, further exploration is essential, particularly during hover, transition, and forward flight phases. Given the varied solutions eVTOL technology provides for addressing climate change and its potential role in urban transportation, this study analyses propeller interactions in a one-after-another configuration. Large Eddy Simulation was employed to understand the intricate multirotor wake structure and its interaction-related behavior.

2 Numerical Setups

2.1 Geometry and Configurations

The TUD-F29 propeller geometry was used in this numerical analysis, which has four blades with a diameter of $D_p = 304.8$ mm and a blade pitch of $beta_0.7R_p = 20$ deg. Fig. 1a depicts the propeller blade geometry. The radius of the hub is $R_h = 0.28R_p$. Fokker Aircraft Company defined this geometry for their internal F29 project, [18]. The F29 propeller was employed in an extensive numerical investigation of propeller aerodynamics and propeller–propeller interaction in an OAA configuration. Its selection was based on the need for coherence in validating the numerical setup with the experimental results presented by Tom Stokkermans [15]. The geometry of the F29 propeller blade and detailed airfoil data are freely accessible as supplementary documents on his ResearchGate account.

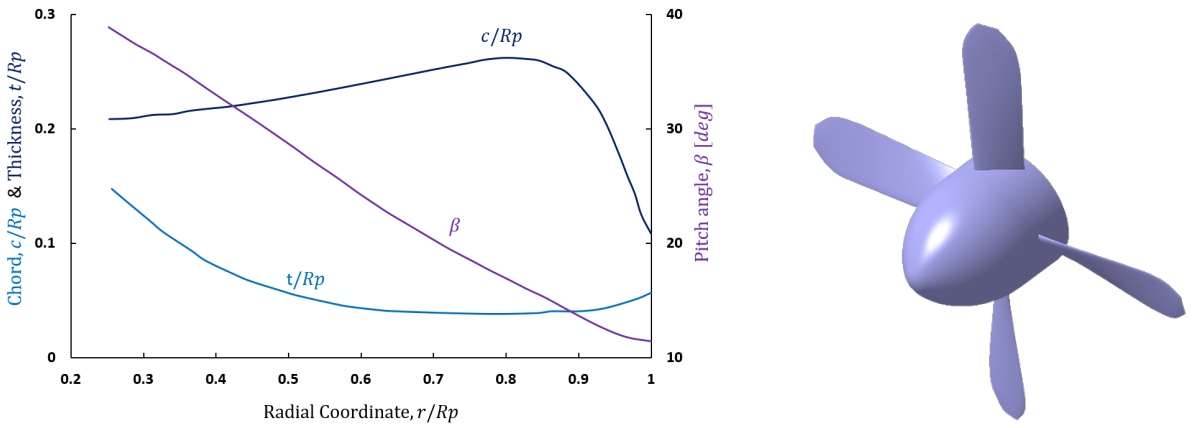

(a) Blade geometry characteristics in radial direction

(b) 3D geometry

FIGURE 1 – F29 propeller geometry details including the a) Blade geometry characteristics in radial direction b) 3D geometry

The multirotor arrangements under consideration, shown in Fig.2, consist of the isolated propeller, as depicted in Fig.2a, and the OAA configuration, as illustrated in Fig.2c and Fig.2b. In this configuration, two propellers are aligned with their axes of rotation in parallel, with a separation of 2.66 times the propeller radius ($2.66R_p$) in the longitudinal direction and 1.4 times the propeller radius ($1.4R_p$) in the lateral direction.

All examined cases have been run with a propeller angle set at zero degrees ($\alpha_p = 0$), i.e the propeller's axis of rotation is aligned in parallel with the incoming freestream flow. The propeller angle, denoted as α_p, represents the angle formed between the rotational axis of the propeller and the horizontal plane.

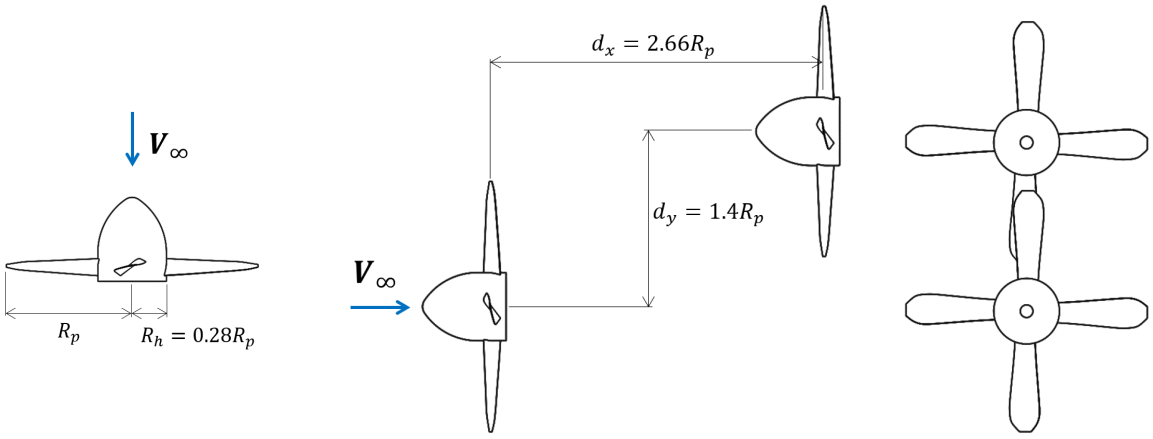

(a) Isolated propeller

(b) Side view of OAA

(c) Front view of OAA

FIGURE 2 – Overview of different test configurations, indicating main dimensions : a) Isolated propeller, b)Side view of OAA c) Front view of OAA

2.2 Computational Domain

The computational domain for numerical solutions depends on specific problem as well as the aerodynamic characteristics of the geometry under investigation. When analyzing a rotating propeller, two domains approach is used, which includes the rotating domain (RD) and the surrounding domain (SD). These domains serve different purposes in properly simulating the behavior of the propeller induced flow and its interaction with the surrounding airflow. The RD is designed to facilitate the modeling of the rotational motion of the propeller through mesh motion. It has a cylindrical shape that envelops each propeller and has a radius that is 1.13 times the propeller radius ($R_{RD} = 1.13Rp$). It also extends 10 mm in the positive x-direction and 20 mm behind the hub. The SD, on

the other hand, is a rectangular parallelepiped that encompasses both the RD and the propeller itself. As depicted in Fig. 3, it extends 10 times and 14 times the propeller radius ($12R_p$) behind the isolated and rear propellers respectively. This setup enables for the visualization of the wake of the propeller and was sufficient to have far boundary and freestream conditions. These dimensions were carefully determined and have been shown to be adequate for the purposes of this study and are in the same order as that employed by Stokkermans [18].

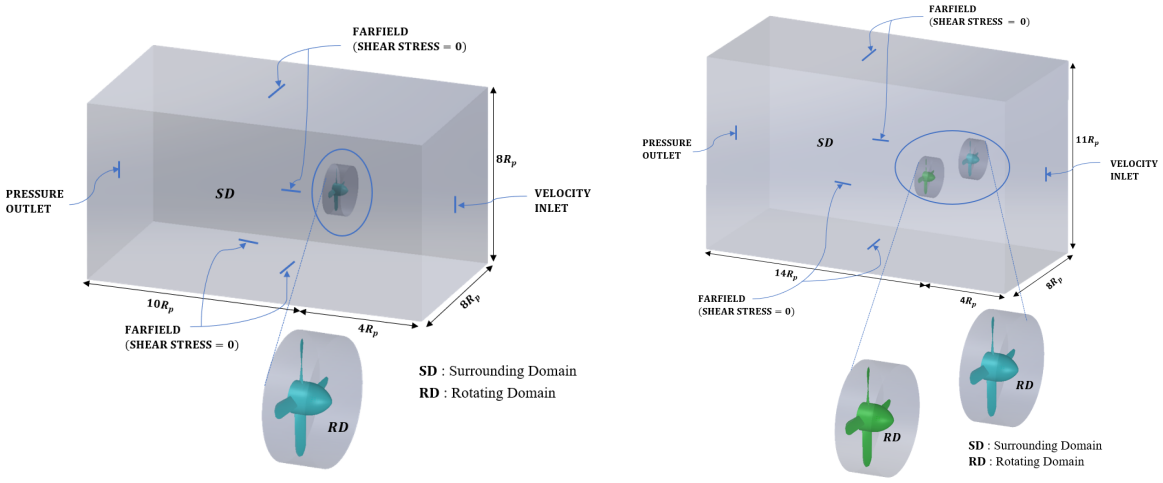

(a) Computational domain of the Isolated propeller

(b) Computational domain of the OAA

FIGURE 3 – Computational domain and boundaries conditions : a) Computational domain of the Isolated propeller b) Computational domain of the OAA cases

2.3 Boundary Conditions

All simulations were performed under the following conditions : a freestream velocity of 20 m/s and an advance ratio (J) ranging from 0.4 to less than 0.7 ($0.4 \leq J < 0.7$) for the isolated propeller. For the propeller– propeller interaction analyses, the simulations were conducted at $V_\infty = 20m/s$ and $J = 0.4$.

The inlet and outlet were configured as a velocity inlet and pressure outlet, respectively, while all other sides of the SD were set as farfield boundaries imposing zero shear stress, as depicted in Fig. 3. A detailed summary of the applied boundary conditions is shown in Table 1.

TABLE 1 – Boundary Conditions

Boundaries	Boundary conditions	Magnitude
Inlet	Velocity Inlet	$V_\infty = 20$ m/s
Outlet	Pressure outlet	Gauge Pressure = 0
Farfield	Wall farfield	Shear Stress= 0
Propeller Blades	No-slip	Velocity = 0

2.4 Mesh Generation and Mesh Independence

Mesh generation plays an important role in the numerical simulation workflow as it governs the degree of fidelity between the simulated results and the real-world phenomena. In this study, an unstructured grid was constructed by means of ANSYS Meshing. The grid density was controlled by face sizing, body sizing, inflation layers with first layer thickness and growth rate. The blades were surrounded by inflation layers with first layer thickness, which serves the purpose of satisfying the requirement of the $y^+ < 1$ of the LES turbulence model. Despite the significant increase in computational cost associated with smaller y^+ values, a $y^+ = 0.8$ was used in conjunction with 20 inflation layers and growth rate of 1.2, as to be able to capture properly the physic and behavior of the flow within the boundary sub-layers of the blades.

Mesh independence study was conducted to ensure that the solution does not depend on the mesh size. This process allows for creating a mesh with sufficient quality to achieve reliable and accurate results while minimizing computational time and achieving good solution convergence. For this purpose, five different meshes, ranging from relatively coarse to very-fine, have been generated, as outlined in Table 2. It's worth noting that in all cases, the

settings for the inflation layer remained consistent, and the condition $y+ < 1$ was maintained. The variations were introduced through domain refinement, with particular attention on critical regions such as the vicinity of the propeller blades and rotating domain. The blades surfaces also was refined as well as the interfaces separating the the rotational domain and stationary domain.

TABLE 2 – Number of elements and nodes of the coarse, medium, med-fine, fine and very-fine meshes

Meshes	Coarse	Medium	Med-fine	Fine	Very-Fine
Elements	755,494	1,159,0645	2,368,645	8,583,596	12,896,061
Nodes	245,933	396,947	853,799	2,368,645	5,056,237

To evaluate the accuracy of each mesh, the thrust coefficient, C_T, and torque coefficient, C_Q were monitored for an average simulation time of 5 rotations. As shown in Fig 4, the variation of the monitored quantities become quasi-static after certain number of elements. The thrust coefficient increases by 1.6% and torque coefficient by 0.07% when the number of elements was increased from 2.4 to 8.6 million, while the variation in both coefficients becomes relatively negligible, with only 0.1% and 0.02% variations, respectively when the number of elements increase from 8.6 to 12.9 million.

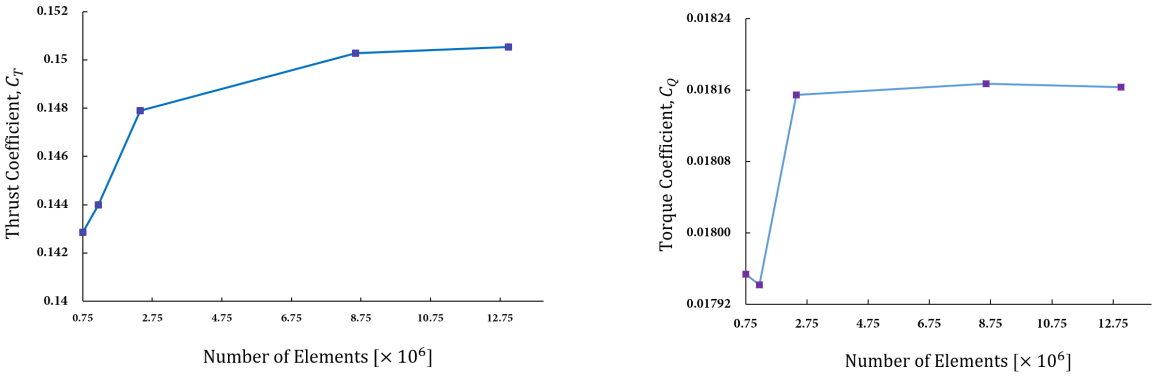

(a) Thrust Coefficient

(b) Mesh independence study for isolated propeller

FIGURE 4 – Mesh independence study for isolated propeller

These results suggest that the 8.6 million-element mesh is sufficient to yield accurate results with reduced computational costs. Detailed mesh setup information for the selected fine mesh element is presented in Table 3, and the mesh structure is illustrated in Fig. 5. Indeed, Fig. 5a displays the inflation layers around the blade. The identical mesh setup was applied to the OAA configuration, with a longitudinal cut view is depicted in Fig. 5b.

TABLE 3 – Mesh setup of the optimal mesh

Mesh options	Parameters
Volume mesh	Tetrahedral
Element size and maximum size	4×10^{-2} m
Minimum face size	4×10^{-4} m
Inflation option	First Layer Thickness
First layer height	1.3×10^{-5} m
Maximum layers/Growth rate	20/1.2

2.5 Governing Equations and Turbulence Model

In this study, the Navier-Stokes (N-S) equations including energy equation are solved using URANS coupled with *SST* $k-\omega$ as a solution starter. Once convergence is achieved, it is superimposed by the LES model. The solver operates under pressure-based transient, considering gravity in negative y-direction. The RD rotates counterclockwise about the x-axis. Air is treated as an ideal gas. The motion of viscous fluid can be described by N-S and energy equations : conservation of mass, momentum and energy.

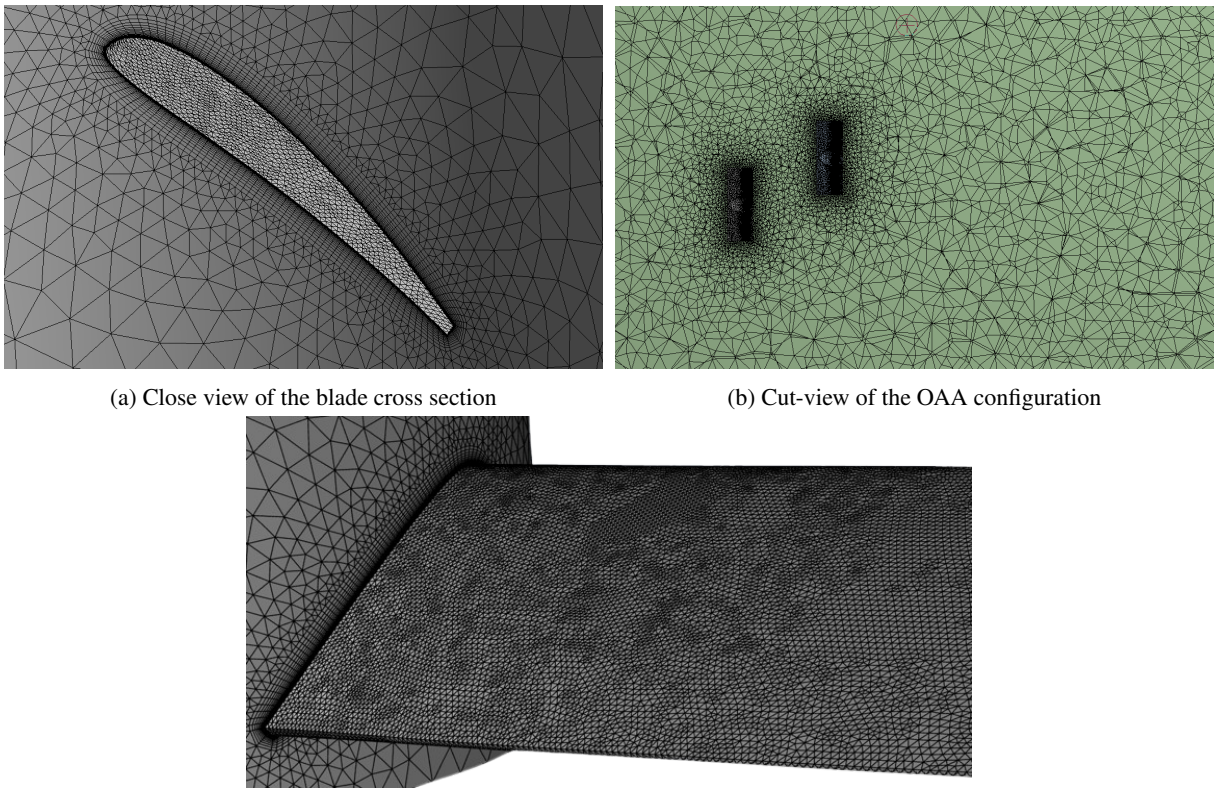

(a) Close view of the blade cross section

(b) Cut-view of the OAA configuration

(c) Close view of the blade surface meshing

FIGURE 5 – Meshing of the computational domain : a) close view of the blade cross section b) Cut-view of the OAA configuration c) Close view of the blade surface meshing

LES Formulation : Filtered N-S equations

Direct Numerical Simulation (DNS) resolves the velocity field $\phi(x,t)$ to the Kolmogorov scale η, while LES deals with a filtered velocity field $\bar{\phi}(x,t)$ on a relatively coarser grid. LES principles, detailed in [26], highlight the role of large eddies in momentum, mass, energy, and scalar transport. Large eddies strongly depend on geometry, while small eddies exhibit isotropic behavior, providing universality. The filtering process removes small eddies, allowing the focus on large eddy dynamics. The filtered function is defined by

$$\bar{\phi}(\mathbf{x},\mathbf{t}) = \int_{\mathcal{D}} \phi(\mathbf{x}') G(\mathbf{x},\mathbf{x}') \, d\mathbf{x}' \tag{1}$$

where $\mathcal{D}$ is the fluid domain and G is the specified filter function that determines scale of resolved eddies and satisfies the normalization condition [27], $\int_{\mathcal{D}} G(\mathbf{x},\mathbf{x}') \, d\mathbf{x}' = 1$.
Filtered N-S equations gives [26]

$$\frac{\partial \rho}{\partial t} + \frac{\partial}{\partial x_i}(\rho \bar{u}_i) = 0 \tag{2}$$

and

$$\frac{\partial}{\partial t}(\rho \bar{u}_i) + \frac{\partial}{\partial x_j}(\rho \bar{u}_i \bar{u}_j) = \frac{\partial}{\partial x_j}(\sigma_{ij}) - \frac{\partial \bar{p}}{\partial x_i} - \frac{\partial \tau_{ij}}{\partial x_j} \tag{3}$$

where σ_{ij} is the stress tensor due to molecular viscosity defined by

$$\sigma_{ij} \equiv \left[\mu\left(\frac{\partial \bar{u}_i}{\partial x_j} + \frac{\partial \bar{u}_j}{\partial x_i}\right)\right] - \frac{2}{3}\mu \frac{\partial \bar{u}_l}{\partial x_l}\delta_{ij} \tag{4}$$

and τ_{ij} is the subgrid-scale stress defined by

$$\tau_{ij} \equiv \rho\overline{\bar{u}_i \bar{u}_j} - \rho \bar{u}_i \bar{u}_j \tag{5}$$

2.6 Physical Setup

A Sliding Mesh also known as mesh motion was employed to compute the unsteady flowfield generated by the propeller. This choice was driven by the high accuracy of the method in addressing the complexities of problems involving moving components [26]. The cell zones in the Sliding Mesh method rotate in defined increments relative to each other along the mesh interface. Given the unsteady nature of the flow in this problem, a transient condition is required to accurately capture the dynamic behavior.

Time Step Calculation

The time step is methodically calculated to precisely capture the flow characteristics of the propeller using LES, taking into account the flow and operating conditions. This careful consideration ensures that the time step is appropriate for resolving the turbulent aspects of the flow, allowing for an accurate representation of the propeller aerodynamic behavior. By selecting an ideal time step, the LES technique may successfully simulate the dynamic and unsteady nature of the flow around the propeller, resulting in reliable and insightful simulations.

The approach given in Ref. [28] is used to calculate the time step size (TSS). The TSS is such that the passing of single blade is divided into 15. Since, the F29 propeller has 4 blades, with given rotational speed ω in rad/s, the TSS is calculated as follow :

$$TSS = \frac{360}{4 \times 15 \times 180\omega/\pi} \tag{6}$$

The $180\omega/\pi$ term in the Equation 6, represents the conversion of the rotational speed from rad/s to deg/s. There are 4 blades, so, each blade period corresponds to 15 times steps. Therefore, a complete one revolution will take $4 \times 15 = 60$ times steps.

Validation of the numerical setup for the isolated propeller

Although the numerical approach provides a powerful tool for the exploration of physical flow phenomena, its reliability is not absolute until it has been validated through experimental testing. Therefore, the simulation model setup was initially subjected to validation against experimental data obtained from research conducted at the Technical University of Delft (TUD) by Stokkermans [18]. The simulations were conducted using the same propeller (F29) under non-zero airspeed conditions, as shown in Fig. 6a and identical operational conditions.

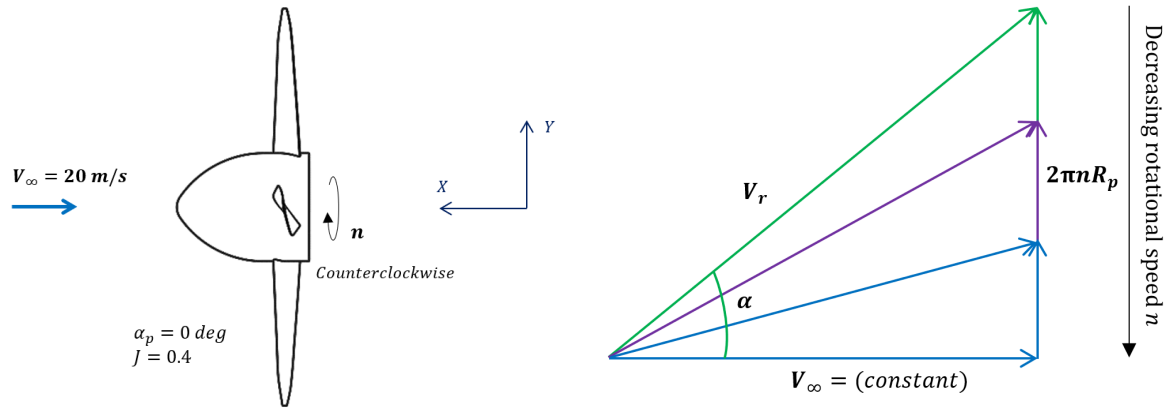

(a) configuration

(b) Velocity triangle with decreasing n

FIGURE 6 – Isolated Propeller : a) Configuration b) Velocity triangle with decreasing n

The Fig. 7, compares the thrust curves obtained from F29 propeller [18], to the current numerical simulations. The results reveal consistent trends with good agreement. The partial disparity in thrust coefficient curves may arise from the potential underestimation of the numerical solver or a potential overestimation of thrust values by the sensors in the experimental measurements, which agrees with the findings of Usai [14]. The average difference between the experimental and numerical predictions for the thrust coefficient is $\Delta C_T = 0.018$. Consequently, these comparisons instill a degree of confidence in the numerical setup accuracy.

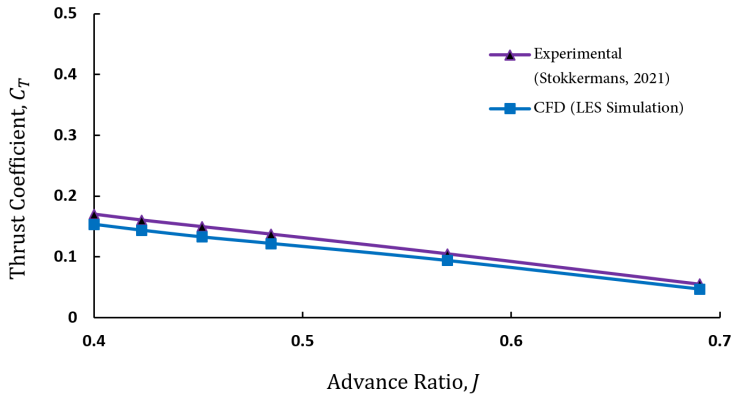

FIGURE 7 – Comparison of the isolated propeller thrust coefficient, obtained from the numerical simulation with experimental data

3 Results and Discussion

To understand the impact of aerodynamic interactions on propeller performance in OAA configuration, the performance of an isolated propeller was evaluated and considered as reference. This served as the baseline against which we compare the performance of each propeller in this configuration. In this section, the term "propeller plane" is used to indicate the plane of rotation of the propeller.

3.1 Propeller Performance Analysis

As depicted in Fig. 7, it is observed that the thrust coefficient, and by extension the thrust, decreases as the advance ratio increases. The advance ratio, denoted as J, is the ratio of the forward speed, V_∞, of the aircraft to the propeller rotational speed, n and diameter, D_p. Consequently, this relationship introduces intricate aerodynamic factors into the equation. At higher advance ratios, where J approaches 1, it means that the aircraft's forward speed is nearly equal to the tangential speed of the propeller tips ($2\pi n R_p$). Given that the diameter of the propeller is constant, variations in J are contingent on changes in V_∞ and n. In this particular study, the forward speed remains constant, while the rotational speed of the propeller decreases as illustrated in Fig. 6b. This decrease in n is implemented to increase J. Consequently, this results in a reduction in the angle of attack on the propeller blades. The reduction in the angle of attack occurs because the altered rotational speed influences the relative airflow over the blades, leading to an angle of attack that is less conducive to efficient thrust generation. As a consequence, the propeller blades operate therefore at angles where they are less able to maintain lift, which results in decreased thrust.

TABLE 4 – Comparison of propeller performance in OAA configuration with isolated configuration for the condition where $J = 0.4$, $\alpha_p = 0$, $d_x/R_p = 2.66$ and $d_y/R_p = 1.4$

	Thrust coefficient	$T_{OAA}/(2T_{iso})$	Power coefficient	$P_{OAA}/(2P_{iso})$
Front propeller	0.147	0.93	0.110	0.94
Rear propeller	0.130		0.099	
Isolated propeller	0.149		0.111	

The OAA configuration considered in this study is characterized by the following specific parameters : $\alpha_p = 0$, $d_x/R_p = 2.66$, and $d_y/R_p = 1.4$. The selection of these values was influenced by the design of the Airbus Vahana eVTOL aircraft [10]. However, the choice of $d_x/R_p = 2.66$ corresponds to half of the distance in the Vahana design. This selection was made deliberately to effectively investigate and measure the effects of propeller–propeller interactions within the current configuration. The two propellers operate at the same advance ratio $J = 0.4$ and rotate counterclockwise (observer facing the propeller from the front). The performance of each propeller is described in Table 4. The overall thrust generated by the OAA configuration is compared with the combined thrust of two isolated propellers, the ratio, indicates a 7% reduction. Similarly, the power ratio in the OAA is reduced by 6%. Therefore, when compared with a single isolated propeller, propellers operating in the OAA arrangement

produce less thrust and power.

The thrust and power coefficients obtained for the front propeller exhibited minimal deviations from those of the isolated propeller. This observation can be attributed to the specific configuration and conditions under which the study was conducted. In essence, the front propeller is located in a region of the flow field where the airflow remains undisturbed. Consequently, the thrust generated by the front propeller is similar to that of an isolated propeller, with the decrease of $\Delta C_{T\,front/iso} = 0.002$, which may be due to the prediction error. In this OAA configuration, the front propeller operated efficiently ; hence, the power required for the front propeller to produce the observed thrust closely aligned with the power needs of an isolated propeller.

In contrast, the rear propeller, which partially overlaps with the front propeller, experiences a reduction of 12.4% ($\Delta C_{T\,rear/iso} = 0.019$) in thrust coefficient and a 10.43% ($\Delta C_{P\,rear/iso} = 0.011$) decrease in power coefficient. These observed reductions is attributed to the non-uniform and turbulent nature of the incoming flow. Indeed, the aft propeller operates within the wake and turbulent flow field generated by the front propeller, which is characterized by the presence of vortices and unsteady flow patterns. This turbulent air introduces disruptions to the otherwise smooth airflow, which is essential for the optimal performance of the aft propeller. The interaction with the wake reduces the effective inflow velocity and lift generation, ultimately decreasing thrust production. In addition, the presence of the front propeller and its associated wake imposes interference drag on the rear propeller. This drag necessitates a higher power input to maintain the same thrust level, resulting in a reduction in power efficiency.

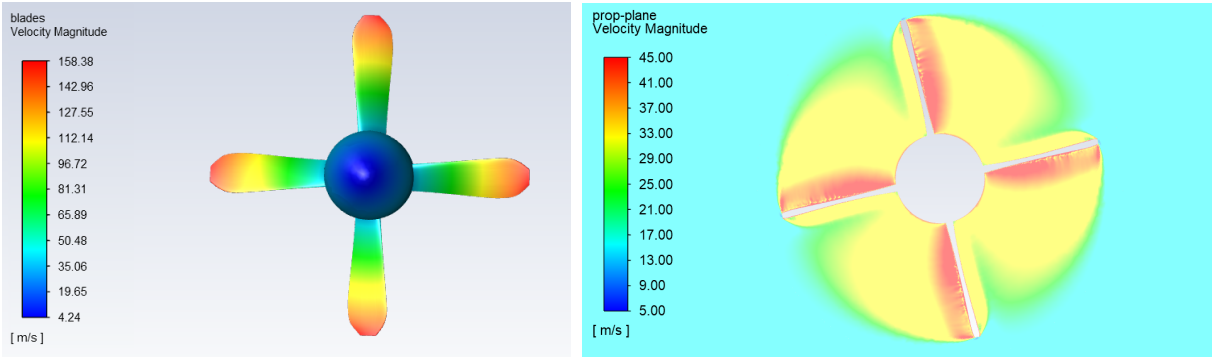

(a) Gradual increase of the velocity over the blades

(b) Rotational plane

FIGURE 8 – Isolated propeller velocity magnitude : a) Gradual increase of the velocity over the blades and b) Rotational plane

3.2 Flow Visualization

The gradual increase in the velocity magnitude over the blades due to the tangential velocity component, is shown in Fig. 8a. The velocity magnitude has lower values near the hub and gradually increases toward the tips of the blades. This is mainly due to the variation in the radius ; however, the lower velocity near the hub can also be associated with the flow interaction with the hub. To effectively visualize and analyze the effect of the interaction on velocity distribution, a specific velocity range of 5–45 m/s was deliberately displayed for all cases. The velocity contour shown in Fig. 8b, serves as a reference for comparing the OAA configuration.

The velocity distribution in the front propeller plane, as illustrated in Fig. 9a, is similar to that of the isolated propeller plane (refer to Fig. 8b). This similarity arises because the front propeller operates in a region that is not affected by presence of the rear propeller. On the other hand, the distribution shown in Fig. 9b, representing the rotational plane of the rear propeller, shows significant differences. It illustrates the merging of the two streamtubes. The airflow from the front propeller, which contains vortices and disturbances created by the rotating blades, impinges on the rear propeller. In particular, the section of the rear propeller that partially overlaps with the front propeller experiences a non-uniform and disturbed flow from the front. This results in a nonuniform distribution of loads over the rear propeller disc. Some sections of the rear propeller receive airflow that is more favorable for generating thrust, whereas others experience less favorable conditions. This non-uniform load distribution can result in a decrease in thrust production. The interaction is clearly observed by examining the slipstream of the two propellers in Fig.9d, which is compared with the case of an isolated propeller in Fig. 9c.

The swirl flow generated by the rotational motion of the two propellers is depicted in Fig. 10 through helicity. Helicity density characterizes helical flow motion and is proportional to the flow strength, vertical wind shear, and

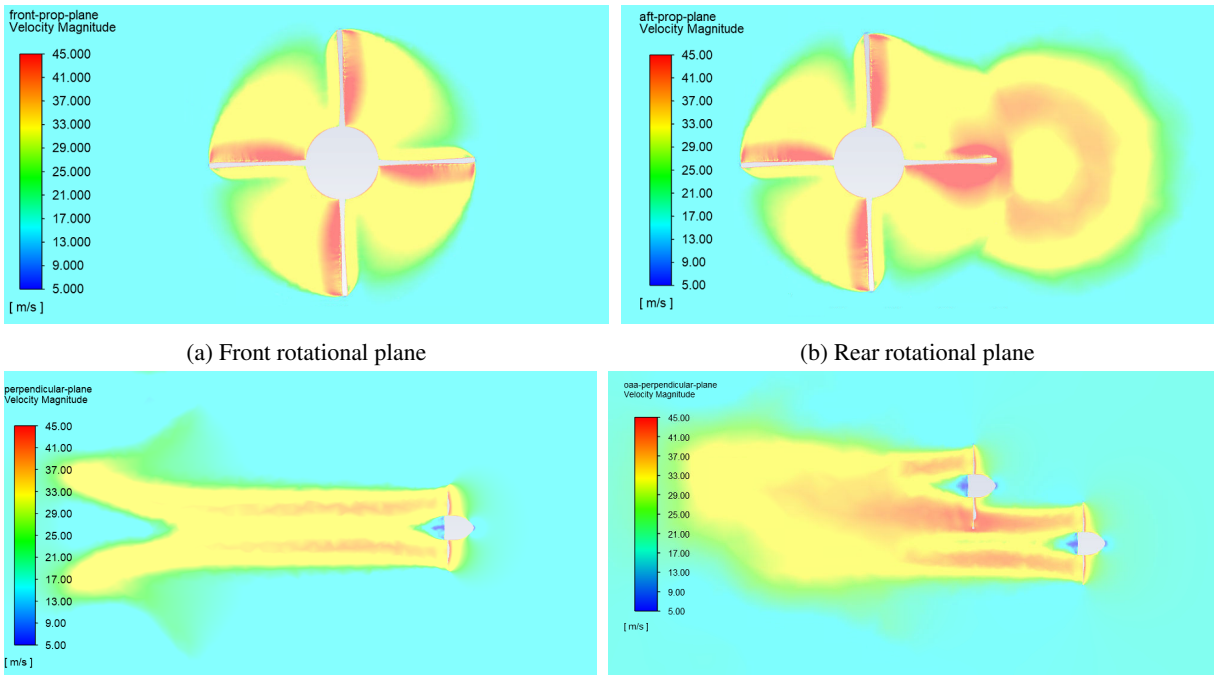

(a) Front rotational plane

(b) Rear rotational plane

(c) Wake region of the isolated case

(d) Wake region of the OAA case

FIGURE 9 – Velocity magnitude distributions in the planes of rotations and wake regions : a) Front rotational plane b) Rear rotational plane c) Wake region of the isolated case and d) Wake region of the OAA case

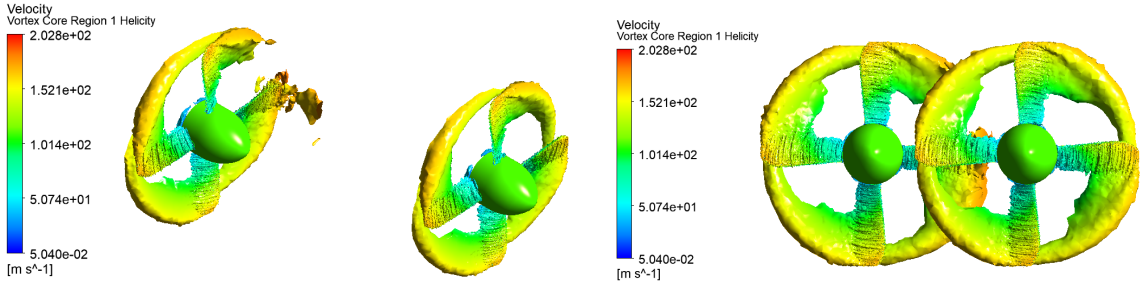

(a) Isometric view

(b) Front view

FIGURE 10 – Visualization of blade vortex Core regions of the OAA configuration by means of helicity with velocity as color variable, level 0.004 a) Isometric view b) Front view

the degree of turning in the flow. This property is defined as the scalar product of the vorticity vector and velocity vector [29]. The front propeller exhibits a regular shape in the turning motion, whereas the rear propeller shows different characteristics. The irregular swirl shape observed on the rear propeller is a result of the accelerated and disturbed incoming flow from the front propeller affecting the part of the rear propeller that is overlapped. The helicity level of 0.004 may be too high to reveal the flow turning clearly at this region. However, reducing the level below that value makes the shape too coarse in other parts of the propellers.

4 Conclusion and Recommendations

A combination of URANS and LES turbulence models was used in this study to evaluate propeller–propeller aerodynamic interactions in an OAA configuration, focusing specifically on a lateral spacing of $1.4R_p$ and a longitudinal spacing of $2.66R_p$ with zero propeller angle, which leads to partial overlap To evaluate the performance penalties caused by these interactions, the results were compared with those of an isolated propeller case. The results reveal a slight difference of $\Delta C_{T\,front/iso} = 0.002$ in the thrust coefficient of the front propeller, which

may be due to the prediction error. The rear propeller, on the other hand, loses 12.4% of its thrust and 10.43% of its power. Therefore, the rear propeller would require more power to develop thrust equal to that of the front one. These reductions are attributed to the disturbed, non-uniform and turbulent inflow imparted on the rear propeller from the wake of the front propeller. The analysis of propellers slipstreams and their interactions provides valuable insight into the intricacies of multirotor aerodynamics. The blockage effect provided by the front propeller on the slipstream of the rear propeller can also change the thrust and torque distributions.

Although the above results provide valuable insights into propeller–propeller interactions for a specific configuration and flight condition, additional analyses should be conducted to explore a broader range of parameters in different flight regimes and configurations. In addition, future efforts should focus on acoustics, structural dynamics, vibrations, and control. Capturing this multiphysics behavior will allow to predict the performance across operating envelopes and integrate design. Nonetheless, this study reveals the complicated interaction between the two propellers and can serve as a benchmark against which to compare novel unconventional propeller designs that aim to mitigate blade tip vortices generation.

Acknowledgment

The authors express gratitude to the LERMA laboratory for providing access to the simulation facilities utilized in this research endeavor.

Nomenclature

eVTOL	Electric Vertical Take-Off and Landing	J	Advance ratio $= V_\infty/(2nR_p)$ $[-]$
DEP	Distributed Electric Propulsion	α_p	Propeller angle $[deg]$
UAM	Urban Air Mobility	ρ_∞	Freestream air density $[kg/m^3]$
LES	Large Eddy Simulation	d_x	Longitudinal spacing $[m]$
OAA	One-After-Another	d_y	Lateral spacing $[m]$
RD	Rotating Domain	V_∞	Freestream velocity $[m/s]$
URANS	Unsteady Reynolds-Averaged Navier-Stokes	n	Propeller revolution per second $[rev/s]$
SD	Surrounding Domain	C_T	Thrust coefficient $= T/(\rho_\infty n^2 {D_p}^4)$ $[-]$
T	Thrust $[N]$	C_Q	Torque coefficient $= Q/(\rho_\infty n^2 {D_p}^5)$ $[-]$
Q	Torque $[N.m]$	C_P	Power coefficient $= P/(\rho_\infty n^3 {D_p}^5)$ $[-]$
P	Power $[Watt]$	R_p	Propeller radius ($2R_p = D_p$) $[m]$

Références

[1] Aleksandar Bauranov and Jasenka Rakas. Designing airspace for urban air mobility : A review of concepts and approaches. *Progress in Aerospace Sciences*, 125(100726), 2021. https://doi.org/10.1016/j.paerosci.2021.100726.

[2] Giuseppe Palaia, Karim Abu Salem, Vittorio Cipolla, Vincenzo Binante, and Davide Zanetti. A conceptual design methodology for e-vtol aircraft for urban air mobility. *Applied Sciences*, 11(10815), 2021. https://doi.org/10.3390/app112210815.

[3] Jeff Holden and Nikhil Goel. Fast-forwarding to a future of on-demand urban air transportation. Technical report, Tech. rep. Uber Elevate, 2016. https://evtol.news/__media/PDFs/UberElevateWhitePaperOct2016.pdf.

[4] Adam Cohen and Susan Shaheen. Urban air mobility : Opportunities and obstacles. *International Encyclopedia of Transportation*, pages Pages : 702–709, 2021. https://doi.org/10.1016/B978-0-08-102671-7.10764-X.

[5] Hyun D. Kim ; Aaron T. Perry and Phillip J. Ansell. A review of distributed electric propulsion concepts for air vehicle technology. Cincinnati, Ohio, July 2018. AIAA/IEE Electric Aircraft Technologies Symposium, IEEE. https://ntrs.nasa.gov/citations/20180004730.

[6] Hyun D. Kim ; Aaron T. Perry and Phillip J Ansell. Progress in distributed electric propulsion vehicles and technologies. Technical report, NTRS - NASA Technical Reports Server, 2020. https://ntrs.nasa.gov/citations/20200011461.

[7] Christopher Courtin ; Ara Mahseredjian ; Annick J. Dewald ; Mark Drela and John Hansman. A performance comparison of estol and evtol aircraft. Online Event, August 2021. American Institute of Aeronautics and Astronautics, ARC. https://doi.org/10.2514/6.2021-3220.

[8] John. D. Anderson. *Aircraft Performance and Design*, chapter 3, 5, 8. WCB McGraw-Hill Education, New York, 1 edition, 2010. https://soaneemrana.org/onewebmedia/AIRCRAFT%20PERFORMANCE%20AND%20DESIGN1.pdf.

[9] Jubilee Prasad Rao, Jonathan E. Holzsager, Marco M. Maia, and Javier F. Diez. Experimental study into optimal configuration and operation of two-four rotor coaxial systems for evtol vehicles. *Aerospace*, 9(252), 2022. https://www.mdpi.com/2226-4310/9/8/452.

[10] Electric VTOL Aircraft News by the Vertical Flight Society (Vertitol). E-vtol aircraft directory. https://evtol.news/aircraft [Accessed : November 7, 2023].

[11] Alessandro Bacchin and Enrico Cestino. Electric vtol configurations comparison. *Aerospace*, 6(26), 2019. https://doi.org/10.3390/aerospace6030026.

[12] Eduardo Alvarez, Austin Schenk, Tyler Critchfield, and Andrew Ning. Rotor-on-rotor aeroacoustic interactions of multirotor in hover. *Journal of the American Helicopter Society*, 2020. https://scholarsarchive.byu.edu/facpub/4053.

[13] William C. Hayes Jr. ; Richard E. Kuhn and Irving R. Sherman. Effects of propellers position and overlap on the slipstream deflection characteristcs of a wing-propellers configuration equipped with a sliding and fowler flap. Technical report, NACA, Langley Aeronautical Laboratory, 1958.

[14] Usai Daniele. Aerodynamic interaction between overlapping propellers, 2019. https://www.researchgate.net/publication/351730719_Aerodynamic_Interaction_Between_Overlapping_Propellers_A_Numerical_and_Experimental_Study.

[15] Tom C. A. Stokkermans, Daniele Usai, Tomas Sinnige, and Leo L. M. Veldhuis. Aerodynamic interaction effects between propellers in typical evtol vehicle configurations. *Journal of Aircraft*, 58, 2021. https://doi.org/10.2514/1.C035814.

[16] Abraham Atte ; Daley Wylie and Juergen Rauleder. Experimental evaluation of multi-rotor aerodynamic interactions. Fort Worth, Texas, July 2022. Vertical Flight Society Forum 78. https://doi.org/10.4050/F-0078-2022-17467.

[17] Riccardo Piccinini, Matteo Tugnoli, and Alex Zanotti. Numerical investigation of the rotor-rotor aerodynamic interaction for evtol aircraft configurations. *Energies*, 2020. https://doi.org/10.3390/en13225995.

[18] Tom Caton Arnaud Stokkermans. *Aerodynamics of Propellers in Interaction Dominated Flowfields : An Application to Novel Aerospace Vehicles*. PhD thesis, Delft University of Technology, 2020. https://pure.tudelft.nl/ws/portalfiles/portal/84548703/Stokkermans_TCA_PhDthesis.pdf.

[19] Alessandro Zarri, Edoardo Dell'Erba, Wim Munters, and Christophe Schram. Aeroacoustic installation effects in multirotorcraft : Numerical investigations of a small-size drone model. *Aerospace Science and Technology*, 128 :107762, 2022. https://doi.org/10.1016/j.ast.2022.107762.

[20] Omer Elsayed, Ashraf A Omar, Ali Jeddi, Saad EL HESSNI, and Fatima Zahra Hachimy. Drag reduction by application of different shape designs in a sport utility vehicle. *International Journal of Automotive and Mechanical Engineering*, 18(3) :8870–8881, 2021. https://doi.org/10.15282/ijame.18.3.2021.03.0680.

[21] Omer A Elsayed, Waqar Asrar, Ashraf A Omar, Kijung Kwon, and Hyejin Jung. Experimental investigation of plain-and flapped-wing tip vortex. *Journal of aircraft*, 46(1) :254–262, 2009. https://doi.org/10.2514/1.38217.

[22] Omer A Elsayed, Waqar Asrar, Ashraf A Omar, and Kijung Kwon. Influence of differential spoiler settings on the wake vortex characterization and alleviation. *Journal of aircraft*, 2010. https://doi.org/10.2514/1.C000258.

[23] Khaoula Qaissi, Omer Elsayed, Mustapha Faqir, and Elhachmi Essadiqi. Performance enhancement analysis of a horizontal axis wind turbine by vortex trapping cavity. *Journal of Energy Resources Technology*, 144(3) :031303, 2022. https://doi.org/10.1115/1.4052980.

[24] Khaoula Qaissi, Omer Elsayed, Mustapha Faqir, and Elhachmi Essadiqi. Aerodynamic optimization of trailing-edge-serrations for a wind turbine blade using taguchi modified additive model. *Energies*, 16(3) :1099, 2023. https://doi.org/10.3390/en16031099.

[25] Khaoula Qaissi, Omer Elsayed, Mustapha Faqir, and Elhachmi Essadiqi. Optimization of the aeroacoustics and aerodynamics of a wind turbine airfoil with serrations using multi-criteria decision making. In *2023 10th International Conference on Recent Advances in Air and Space Technologies (RAST)*, pages 1–5. IEEE, 2023. https://ieeexplore.ieee.org/document/10197890.

[26] ANSYS. *ANSYS Fluent Theory Guide*. Release 12.0 © ANSYS, Inc, 2009. https://www.afs.enea.it/project/neptunius/docs/fluent/html/th/node1.htm.

[27] Stephen B. Pope. *Turbulent Flows*. Cambridge University Press, 2000. https://www.cambridge.org/highereducation/books/turbulent-flows/C58EFF59AF9B81AE6CFAC9ED16486B3A#overview.

[28] ANSYS. *ANSYS Fluent Tutorial Guide*. Release 18.0, ANSYS, Inc. and ANSYS Europe, 2017.

[29] L.L.M. Veldhuis. *Propeller Wing Aerodynamic Interference*. PhD thesis, PhD, Delft University of Technology, 2005.